Unidirectional luminescence from InGaN/GaN quantum-well metasurfaces

Prasad P. Iyer[1,5], Ryan A. DeCrescent[2,5], Yahya Mohtashami[1], Guillaume Lheureux[3,4], Nikita A. Butakov[1], Abdullah Alhassan[3,4], Claude Weisbuch[3,4], Shuji Nakamura[1,3,4], Steven P. DenBaars[1,3,4] and Jon. A. Schuller[1✉]

III–nitride light-emitting diodes (LEDs) are the backbone of ubiquitous lighting and display applications. Imparting directional emission is an essential requirement for many LED implementations. Although optical packaging[1], nanopatterning[2,3] and surface roughening[4] techniques can enhance LED extraction, directing the emitted light requires bulky optical components. Optical metasurfaces provide precise control over transmitted and reflected waveforms, suggesting a new route for directing light emission. However, it is difficult to adapt metasurface concepts for incoherent light emission, due to the lack of a phase-locking incident wave. Here, we demonstrate a metasurface-based design of InGaN/GaN quantum-well structures that generate narrow, unidirectional transmission and emission lobes at arbitrary engineered angles. We further demonstrate 7-fold and 100-fold enhancements of total and air-coupled external quantum efficiencies, respectively. The results present a new strategy for exploiting metasurface functionality in light-emitting devices.

LEDs are rapidly enabling solid-state solutions to commercial lighting applications. Imparting unidirectionality to LEDs is a challenging problem with a host of applications[5–7] awaiting a scalable solution. Directional emission is naturally observed in lasing systems[8,9], where all of the resonators are emitting coherently. At infrared frequencies, directional thermal emission has been achieved through coupling to nanoantennas[10] and gratings[11,12] via surface waves. At visible frequencies, researchers can direct incoherent light emission from ensembles of point sources through, for example, coupling to optical nanoantennas[13–19]. In Yagi–Uda optical antenna arrays[13–16] and metasurfaces[17], asymmetric emission is achieved through phasing between different nanoantenna elements. However, requirements for precise positioning, and challenges of achieving high emitter densities, often preclude scaling to large areas[18]. Moving beyond these initial demonstrations, greater control over emission directionality may be possible using extended phased-array metasurface concepts[20–22]. For instance, phased-array lensed thermal emission has recently been theoretically demonstrated[12,23]. Such directed thermal emitters typically exploit a peaked local density of optical states (LDOS) and losses associated with surface waves. These absorption losses are necessary for thermal emitters and constrain the applicability to visible-frequency LEDs. Spatially uniform metasurface arrays have been used to enhance[24–27] and control the spectral line shapes[28,29] of incoherent emitters by coupling to specific nanoantenna resonances[17,30,31]. While such

systems often exhibit highly directed emission, uniform structuring necessarily leads to symmetric radiation patterns and precludes the possibility of generating arbitrary phased-array metasurface functionality desirable for future applications. Thus far, there have been no demonstrations of unidirectional photoluminescence (PL) enabled through coupling to extended phased-array metasurfaces. Here, we experimentally demonstrate asymmetric and unidirectional visible-frequency luminescence from incoherent light-emitting phased-array metasurfaces. Furthermore, we demonstrate approximately 7-fold and 100-fold enhancements of the PL external quantum efficiencies (EQE) for total and air-coupled emission, respectively.

Traditional metasurfaces transform a coherent wave by imprinting a sub-wavelength spatial phase profile, $\varphi(x,y)$, across the surface through resonant interaction with plasmonic or dielectric resonators[32–34]. Consider a transmitting metasurface designed to redirect an incident plane wave (with in-plane momentum $|\mathbf{k}_{||,i}| = k_0\sin\theta_i$, where θ_i is the angle of incidence) to an output plane wave (at $|\mathbf{k}_{||,t}| = k_0\sin\theta_t$, where θ_t is the angle of exitance) according to the grating equation, $\mathbf{k}_{||,t} = \mathbf{k}_{||,i} + \mathbf{k}_M$ (ref. [34]). Here, $\mathbf{k}_M = \nabla\varphi$ is the desired in-plane 'metasurface momentum' to be imparted to a transmitting wave and $k_0 = 2\pi/\lambda$ is the free-space momentum of light with wavelength λ. Our passive transmitting metasurface (Fig. 1a) is designed to be compatible with a light-emitting InGaN/GaN multiple quantum wells (QWs) structure grown by metal-oxide chemical vapour deposition on a double-side polished sapphire substrate (see Methods). InGaN QWs are grown at a height $h_{QW} = 1.35\,\mu m$ above the substrate where the GaN defect density is markedly reduced, followed by a 100-nm GaN capping layer, yielding a total film thickness of $h = 1.45\,\mu m$. We directly structure this film into arrays (periodicity, $p = 250\,nm$) of high-aspect-ratio nanopillars (Fig. 1b; see Methods). The metasurface phase, $\varphi(x)$, is controlled by varying the nanopillar widths, w ($h/w = 5.5$–8.5). However, rather than simulate the transmission phase of an incident beam, we simulate the accumulated phase of light emitted into the substrate from in-plane oriented point dipoles located 100 nm below the top of the GaN nanopillars. The finite-difference time-domain (FDTD) simulations assume that the point dipole sources are radiating in-phase with respect to each other, such that they only emit along the surface normal, in analogy with typical transmission/reflection simulations that only consider normal-incidence illumination, transmission and reflection. The numerically calculated emission phase and normalized amplitude are shown in Fig. 1c; 0 to 2π phase control is achieved by
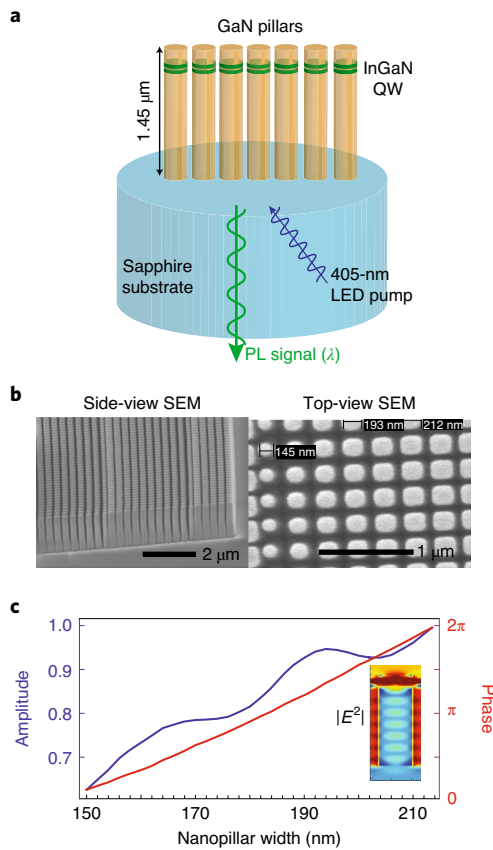
Fig. 1 | Metasurface schematics and design. a, Illustration of the GaN nanopillar system with InGaN multiple QWs (green) grown on a GaN base layer on a double-side polished sapphire substrate. In our experiments, samples are optically pumped using a 405-nm LED and emitted PL is collected from within the substrate using momentum-resolved (that is, Fourier) imaging techniques. **b**, Scanning electron microscopy (SEM) images of a GaN metasurface showing the high-aspect-ratio nanopillars formed with a well-defined size gradient only along the x direction. **c**, The phase (red, right axis) and normalized amplitude (blue, left axis) of the light emitted into the substrate from the point in-plane (x,y) electric dipole embedded in the GaN nanopillar as a function of the nanopillar width. The inset shows a characteristic electric field intensity ($|E^2|$) profile of the excited mode by the point dipole with red (blue) representing maximum (minimum) in field intensity.

varying nanopillar width between 150–210 nm. With this emission phase, we map the required spatial phase profile for beam deflection (based on the grating equation) to the expected nanopillar width at each point on the metasurface. We construct and demonstrate metasurfaces to deflect normal-incidence ($|\mathbf{k}_{\parallel,i}| = 0$) light into desired transmission lobes within the sapphire substrate ($|\mathbf{k}_{\parallel,t}/k_0|$ between 0.17 to 0.98, or equivalently θ_t between 10–80° in air), and subsequently measure the transmission and PL from InGaN QWs embedded within the metasurface nanopillars.

High-efficiency, polarization-independent unidirectional metasurface transmission lobes are measured via energy-momentum spectroscopy[35–37] (see Methods) and are shown in Fig. 2a,b. The momentum-resolved transmission of normal-incidence 540-nm light is plotted as a function of the normalized in-plane electromagnetic momentum, $|\mathbf{k}_{\parallel,t}/k_0|$. Accordingly, the circle $|\mathbf{k}_\parallel/k_0| = 1$ forms the light cone of free-space emission modes, outside of which modes are trapped within the substrate ($1 < |\mathbf{k}_\parallel/k_0| < n_{sub}$; $n_{sub} = 1.77$) or the GaN thin film ($n_{sub} < |\mathbf{k}_\parallel/k_0| < n_{GaN}$; $n_{GaN} \approx 2.2$), where n_{sub} and

n_{GaN} refer to the substrate and GaN refractive indices, respectively. For both s-polarized (Fig. 2a) and p-polarized (Fig. 2b) light, the normal-incidence beam is deflected into a very narrow unidirectional transmitted lobe at the design momentum $\mathbf{k}_{\parallel,t} = \mathbf{k}_M$.

Because the emitting QWs naturally emit over a broad angular range (Supplementary Fig. 3), it is unclear how the metasurface patterning will affect overall luminescence. Energy-momentum spectra of PL from the optically pumped (see Methods) metasurfaces are shown in Fig. 2c,d. The s-polarized PL (Fig. 2c) shows subtle signatures of directional emission, but overall is relatively flat and featureless for all metasurface designs. In contrast, the p-polarized PL predominantly emits into a single very strong unidirectional lobe with in-plane momentum defined approximately by $|\mathbf{k}_\parallel| = -k_0 + k_M$ (Fig. 2d). Consequently, as we increase $|\mathbf{k}_M|$ to steer the transmitted beam from $|\mathbf{k}_\parallel| = 0$ to larger momenta, we see that a strong and unidirectional p-polarized PL lobe is translated from $|\mathbf{k}_\parallel/k_0| = 1$ to smaller momenta (Fig. 2d). Unlike uniform nanopillar arrays[3,24,26,38], we break the inherent symmetry of the emission pattern by introducing a linear phase gradient. The emission is highly directed with a full-width at half-maximum (FWHM) less than $\pm 0.12k_0$ ($\pm 7°$ in air). These results demonstrate the promise for redirecting PL into desired metasurface channels, but the observed polarization dependence highlights the complexity of this phenomenon and the need to better understand its origins.

To better understand the observed emission properties, we develop a simple model starting from analytical calculations of the momentum-dependent emission (the LDOS) from an unstructured film. p-polarized light emission from the unstructured film—which only comes from in-plane oriented dipoles—is 'naturally' concentrated in emission lobes just beyond the critical angle ($|\mathbf{k}_\parallel/k_0| = 1$) that ordinarily are trapped within the substrate (Supplementary Section 3). These relatively sharp p-polarized emission maxima are a consequence of the approximate $\lambda/2n_{GaN}$ (100 nm) distance of the emitter from the GaN/air interface. These intrinsically narrow, but symmetric, emission lobes in turn produce even narrower and asymmetric emission lobes after interacting with the metasurface structure. To understand this phenomenon, we consider a simple model that accounts for both the metasurface microperiodicity, p ($p = 250$ nm is the inter-pillar spacing), and macroperiodicity, P, which depends on the 2π phase wrapping distance, which varies between each metasurface. This microperiodicity along the $\hat{x}$ and $\hat{y}$ directions defines a momentum, $G_0 = 2\pi/p$, that couples wave vectors $\mathbf{k}_\parallel$ to the harmonics $\{\mathbf{k}_\parallel \pm G_0\hat{x}\}$ and $\{\mathbf{k}_\parallel \pm G_0\hat{y}\}$ (ref. [3]); a new LDOS thus accounts for this microperiodicity by summing the original LDOS over a grid of points in k-space separated by $\pm G_0$ along both $\hat{x}$ and $\hat{y}$ axes (Supplementary Fig. 3). The ratio $G_0/k_0 \approx 2.15$ makes the bright thin-film emission lobes between neighbouring zones strongly overlap along the k_x axis, producing bright, narrow emission lobes near the critical angle ($|k_x/k_0| = 1$). We then shift the resultant summed LDOS by an asymmetric metasurface component, $\mathbf{k}_M = +2\pi/P\hat{x}$, along the direction of the phase gradient (Supplementary Fig. 3).

A comparison of experimental far-field PL images (left panels) with our analytical LDOS model (right panels) is made in Fig. 3. The PL is collected with an x-oriented polarizer such that line cuts along $k_x = 0$ ($k_y = 0$) are purely p-polarized (s-polarized). Our simple model very well captures the location, shape and width of the observed directional emission lobes across the five displayed metasurfaces for both polarizations. This excellent agreement between calculations and experiments validates the basic premises of our metasurface design and analytical model, providing insight into how to design future metasurface-modified light emitters. In essence, when emitting light, the metasurface behaves as if it is illuminated at the critical angle, explaining the observed difference in the location of transmission and emission lobes. Overall, these results highlight the importance of starting with a highly directional
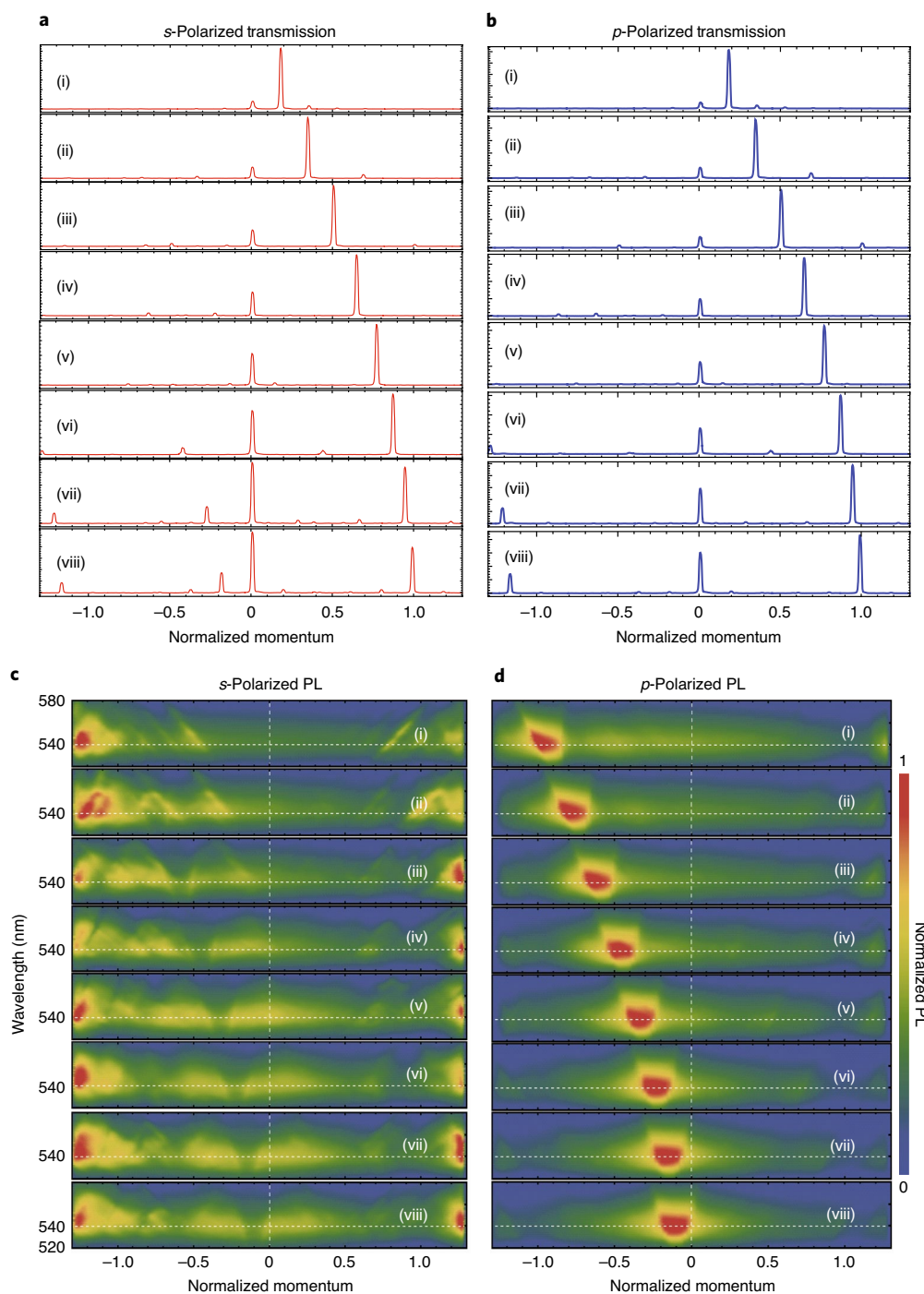
Fig. 2 | Directional metasurface transmission and emission. a,b, *s*- and *p*-polarized transmission through eight distinct metasurfaces as a function of the normalized in-plane momentum ($k_{||}/k_0$). The metasurface design deflects a normally incident beam (0°; $k_{||} = 0$) to a transmitted beam ranging between $k_{||}/k_0 = 0.17$ (10° in air; (i)) to $k_{||}/k_0 = 0.98$ (80° in air; (viii)) using a linear phase profile. Comparing the specular transmission ($k_{||}/k_0 = 0$) to the deflected beam ($k_{||}/k_0 > 0$) illustrates the relative efficiency of the metasurface (see for example Fig. 4a). **c,d,** *s*- and *p*-polarized PL as a function of wavelength (*y* axis, 520–580 nm) and normalized in-plane momentum ($k_{||}/k_0$; *x* axis) for the eight different metasurfaces (one in each panel, (i)–(viii)). Data in each panel have been normalized such that the maximum PL in each plot is equal to unity. The *p*-polarized PL peak is shifted in momentum space from −1 to 0 based on the metasurface design.

LDOS before patterning and considering the effects of both micro- and macroperiodicities.

We quantify the 'beam efficiencies' for GaN metasurfaces (Fig. 4a) operating in both PL (left panel) and transmission (right panel) modes at the peak wavelength. PL beam efficiency is defined as the fraction of total light intensity collected within one FWHM

along the k_x axis (see Methods). Note that, by this definition, the maximum possible PL beam efficiency is less than 1 (for example 0.76 for a perfect Gaussian beam with no side lobes). Transmission beam efficiency is defined as the fraction of total light lettensity collected within local minima immediately flanking the main peak. In transmission, the metasurfaces exhibit up to 80% efficiency
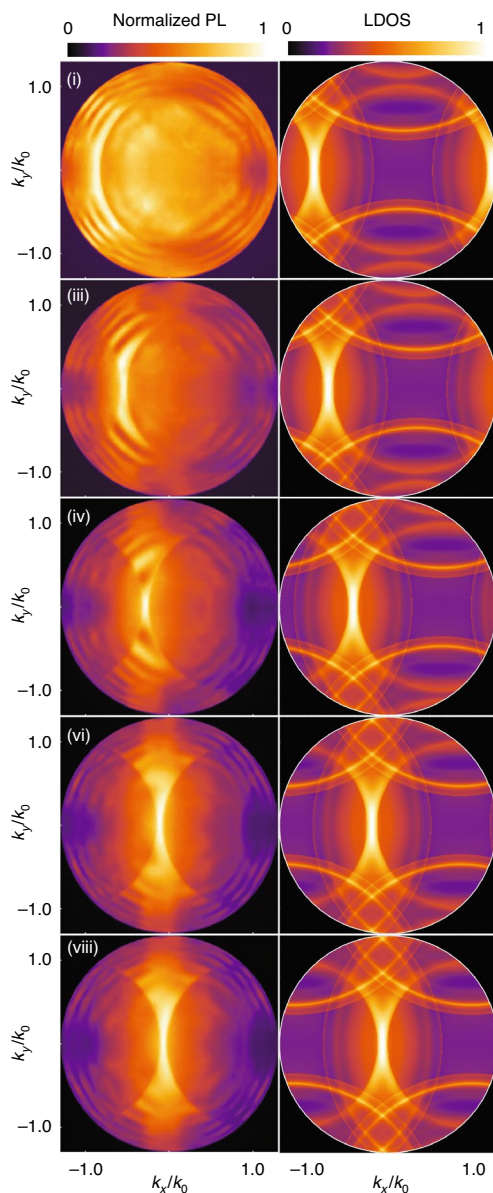
Fig. 3 | Comparison between calculated and measured metasurface radiation patterns. Left: experimental momentum-resolved PL as a function of normalized momenta $\{k_x, k_y\}/k_0$. Light along the k_x (k_y) axis is p- (s-) polarized. Data in each panel have been normalized such that the maximum PL in each plot is equal to unity. Each panel ((i)–(viii)) corresponds to a metasurface design from Fig. 2. The strong PL peak at $k_x = -1$ (in units of k_0) (i) shifts toward $k_x = 0$ (viii) due to the linear metasurface phasing along the x axis. Right: calculated LDOS (normalized radiation rates) based on our model incorporating photonic-crystal effects and metasurface-induced k_x translation. The circular features and the intense asymmetric emission maximum along the k_x axis agree very well with the experimental data (left panels).

for small deflection angles with the efficiency dropping close to 50% for near-grazing transmission. In PL, the metasurfaces similarly show higher efficiency for near-normal emission (up to 40%) with reduced efficiencies for near-grazing emission angles. This efficiency fall-off in transmission has been previously studied in other gratings and metasurfaces[39,40] suggesting that more complex unit-cell designs may be leveraged for higher efficiencies at steeper angles. Remarkably, most (~70–80%) of the light emitted at the

PL peak is polarized along the metasurface gradient for all of the metasurfaces (Fig. 4b and Supplementary Fig. 7), that is, our metasurfaces naturally produce highly polarized directional lobes. This may be particularly useful for micro- and nano-LED displays where external polarizers are applied, leading to a 50% reduction in efficiency for unpolarized emitters[41–43].

In addition to controllable directivity, emitting metasurfaces show a dramatic increase in PL intensity when compared with as-grown films. Across the set of fabricated metasurfaces, total PL collected within the light escape cone ($k_{\parallel} < 1$, EQE$_{air}$) is enhanced by factors of 130–250 when compared with as-grown thin films (Supplementary Section 1). Notably, this is larger than the enhancements measured for uniform nanopillar arrays (factors of ~60–130, Supplementary Fig. 1.1) fabricated with the same material and processes, indicating that metasurfaces enhance EQEs better than comparable photonic crystals. To better understand the origin of these large PL enhancements, we perform detailed measurements of absorption and quantum yields, combined with finite-difference calculations (see Methods and Supplementary Section 1). Measurements, supported by numerical calculations, indicate that increased absorption at the pump wavelength accounts for at most a factor of 2.5 in the observed PL enhancements (Supplementary Figs. 1.1 and 1.2). Therefore, taking measured absorption enhancements into account, an outstanding factor of ~90–150 in the measured EQE$_{air}$ enhancement is attributable to a combination of improved photon extraction and improved internal quantum efficiency. The PL enhancement is concomitant with a substantial blueshift (~160 meV) of the peak emission to 540 nm (Fig. 4c; solid coloured lines). A strain-induced piezoelectric field in the InGaN QWs, leading to a quantum-confined Stark effect, relaxes during the formation (dry etching) of the nanopillars, leading to a higher recombination energy, increased electron–hole wave-function overlap in the QWs (Supplementary Section 5)[44,45] and increased radiative recombination rates. Such strain relaxation may also reduce non-radiative recombination at structural defects, further increasing quantum efficiencies[45,46].

To further decouple variations in optical and material effects in our metasurfaces, we measure the total EQE, that is, across the full 4π solid angle (EQE$_{tot}$), by performing pump-power-dependent PL measurements in an integrating sphere (see Methods). The metasurface EQE$_{tot}$ exceeds, by a factor of ~6–9, the thin films for all pump powers measured (Fig. 4d). Further, measured EQE$_{tot}$ values are comparable to state-of-the-art GaN-based nano-LEDs emitting at 540 nm (ref. [44]). The observed improvements are probably related to the aforementioned strain relaxation effects observed in our structures. Taken together, these results suggest that metasurface patterning improves both photon extraction and the internal quantum efficiency. These notable improvements are particularly promising for addressing the low quantum efficiencies of green-emitting nitride-based emitters[44,47]. This combination of new functionality (that is, controllable directionality) and substantially improved quantum efficiencies and photon extraction may provide major benefits for future LED technologies. This methodology may be further adapted to produce PL with focused spots, or other highly engineered waveforms.

The results presented here demonstrate that metasurface design methodologies may be used to enhance and engineer the luminescence from QW systems. We demonstrate that QW emitting layers strategically embedded within the metasurface elements couple strongly to the metasurface design, thus emitting polarized, unidirectional light by breaking the inherent symmetry conditions of traditional photonic crystals. Fundamentally, we have demonstrated that the same design principles used to direct phase-coherent incident sources can used to direct incoherent light emission. New functionality is complemented by substantial enhancements of photon output through improvements in photon extraction and
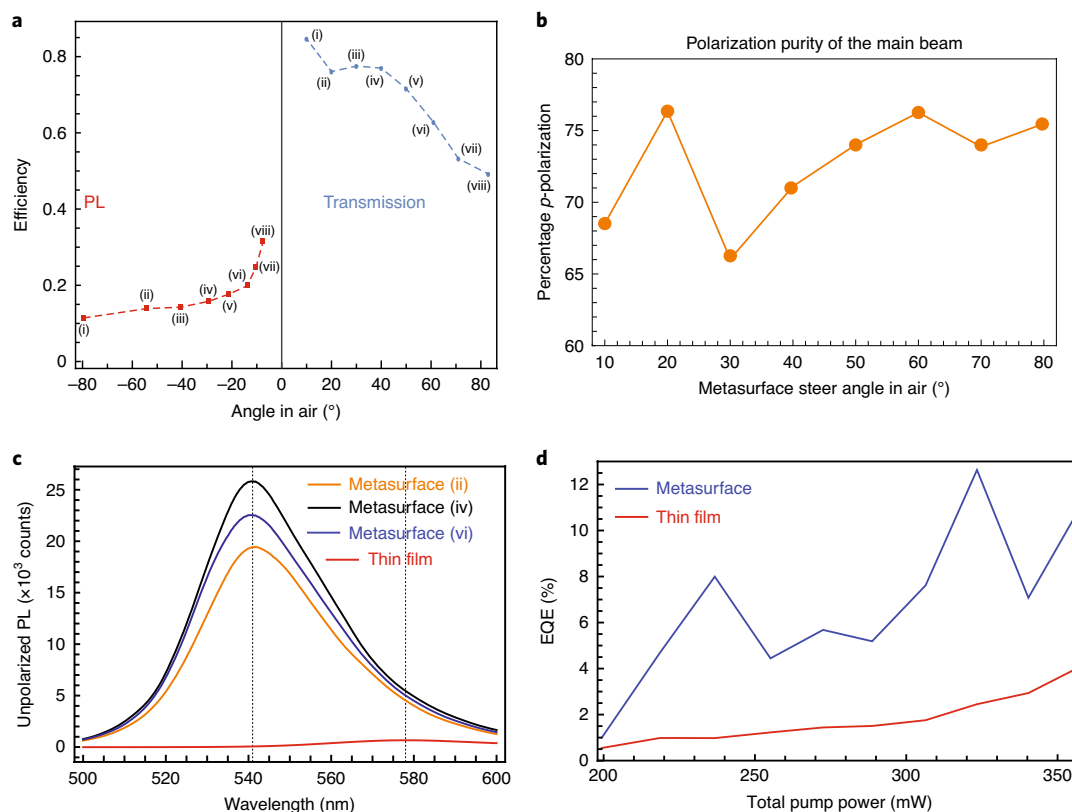
Fig. 4 | Metasurface polarization and efficiency. a, The 'beam efficiency' (portion of power in the main lobe to total collected power at the PL peak wavelength) of transmission (right, blue) and PL (left, red) for all metasurfaces, specified by their design angle. **b**, The percentage polarization of the steered main lobe as a function of the metasurface transmission steer angle (in air). Every point on the curves in **a** and **b** corresponds to a specific designed metasurface plotted in Fig. 2. **c**, PL (integrated over an NA = 1) spectra of metasurfaces and as-grown thin film (red) showing the blueshift and intensity increase achieved through the formation of nanopillars. **d**, EQE measured from the as-grown thin film (red) and metasurface (device (i), blue) as a function of total optical pump power.

strain relaxation. These results point the way to new classes of metasurface-based light emitters where enhanced and directional emission is attained without external packaging components.

Online content

Any methods, additional references, Nature Research reporting summaries, source data, extended data, supplementary information, acknowledgements, peer review information; details of author contributions and competing interests; and statements of data and code availability are available at https://doi.org/10.1038/s41566-020-0641-x.

References

1. Steigerwald, D. A. et al. Illumination with solid state lighting technology. *IEEE J. Sel. Top. Quantum Electron.* **8**, 310–320 (2002).
2. Keller, S. et al. Optical and structural properties of GaN nanopillar and nanostripe arrays with embedded InGaN/GaN multi-quantum wells. *J. Appl. Phys.* **100**, 054314 (2006).
3. Wierer, J. J., David, A. & Megens, M. M. III–nitride photonic-crystal light-emitting diodes with high extraction efficiency. *Nat. Photon.* **3**, 163–169 (2009).
4. Fujii, T. et al. Increase in the extraction efficiency of GaN-based light-emitting diodes via surface roughening. *Appl. Phys. Lett.* **84**, 855–857 (2004).
5. Craford, M. G. LEDs for solid state lighting and other emerging applications: status, trends, and challenges. *Proc. SPIE* **5941**, 594101 (2005).
6. Liu, Z., Chong, W. C., Wong, K. M. & Lau, K. M. GaN-based LED micro-displays for wearable applications. *Microelectron. Eng.* **148**, 98–103 (2015).
7. Huang, J.-J., Kuo, H.-C. & Shen, S.-C. *Nitride Semiconductor Light-emitting Diodes (LEDs): Materials, Technologies, and Applications* (Woodhead Publishing, 2017).
8. Ha, S. T. et al. Directional lasing in resonant semiconductor nanoantenna arrays. *Nat. Nanotechnol.* **13**, 1042–1047 (2018).
9. Hoang, T. B., Akselrod, G. M., Yang, A., Odom, T. W. & Mikkelsen, M. H. Millimeter-scale spatial coherence from a plasmon laser. *Nano Lett.* **17**, 6690–6695 (2017).
10. Schuller, J. A., Taubner, T. & Brongersma, M. L. Optical antenna thermal emitters. *Nat. Photon.* **3**, 658–661 (2009).
11. Sakr, E., Dhaka, S. & Bermel, P. Asymmetric angular-selective thermal emission. *Proc. SPIE* **9743**, 97431D (2016).
12. Inampudi, S., Cheng, J., Salary, M. M. & Mosallaei, H. Unidirectional thermal radiation from a SiC metasurface. *J. Opt. Soc. Am. B* **35**, 39–46 (2018).
13. Curto, A. G. et al. Unidirectional emission of a quantum dot coupled to a nanoantenna. *Science* **329**, 930–933 (2010).
14. Kosako, T., Kadoya, Y. & Hofmann, H. F. Directional control of light by a nano-optical Yagi–Uda antenna. *Nat. Photon.* **4**, 312–315 (2010).
15. Ho, J. et al. Highly directive hybrid metal–dielectric Yagi-Uda nanoantennas. *ACS Nano* **12**, 8616–8624 (2018).
16. Muhlschlegel, P. Resonant optical antennas. *Science* **308**, 1607–1609 (2005).
17. Langguth, L., Schokker, A. H., Guo, K. & Koenderink, A. F. Plasmonic phase-gradient metasurface for spontaneous emission control. *Phys. Rev. B* **92**, 205401 (2015).
18. Hancu, I. M., Curto, A. G., Castro-López, M., Kuttge, M. & van Hulst, N. F. Multipolar interference for directed light emission. *Nano Lett.* **14**, 166–171 (2013).
19. Vaskin, A., Kolkowski, R., Koenderink, A. F. & Staude, I. Light-emitting metasurfaces. *Nanophotonics* **8**, 1151–1198 (2019).
20. Arbabi, E., Arbabi, A., Kamali, S. M., Horie, Y. & Faraon, A. Controlling the sign of chromatic dispersion in diffractive optics with dielectric metasurfaces. *Optica* **4**, 625 (2017).

21. Arbabi, A., Horie, Y., Bagheri, M. & Faraon, A. Dielectric metasurfaces for complete control of phase and polarization with subwavelength spatial resolution and high transmission. *Nat. Nanotechnol.* **10**, 937–943 (2015).
22. Iyer, P. P., Pendharkar, M. & Schuller, J. A. Electrically reconfigurable metasurfaces using heterojunction resonators. *Adv. Opt. Mater.* **4**, 1582–1588 (2016).
23. Chalabi, H., Alù, A. & Brongersma, M. L. Focused thermal emission from a nanostructured SiC surface. *Phys. Rev. B* **94**, 094307 (2016).
24. Liu, S. et al. Light-emitting metasurfaces: simultaneous control of spontaneous emission and far-field radiation. *Nano Lett.* **18**, 6906–6914 (2018).
25. Vaskin, A. et al. Manipulation of magnetic dipole emission from Eu^{3+} with Mie-resonant dielectric metasurfaces. *Nano Lett.* **19**, 1015–1022 (2019).
26. Lozano, G., Grzela, G., Verschuuren, M. A., Ramezani, M. & Rivas, J. G. Tailor-made directional emission in nanoimprinted plasmonic-based light-emitting devices. *Nanoscale* **6**, 9223–9229 (2014).
27. Li, J., Verellen, N. & Van Dorpe, P. Enhancing magnetic dipole emission by a nano-doughnut-shaped silicon disk. *ACS Photon.* **4**, 1893–1898 (2017).
28. Staude, I. et al. Shaping photoluminescence spectra with magnetoelectric resonances in all-dielectric nanoparticles. *ACS Photon.* **2**, 172–177 (2015).
29. Vaskin, A. et al. Directional and spectral shaping of light emission with Mie-resonant silicon nanoantenna arrays. *ACS Photon.* **5**, 1359–1364 (2018).
30. Cotrufo, M., Osorio, C. I. & Koenderink, A. F. Spin-dependent emission from arrays of planar chiral nanoantennas due to lattice and localized plasmon resonances. *ACS Nano* **10**, 3389–3397 (2016).
31. Guo, K., Du, M., Osorio, C. I. & Koenderink, A. F. Broadband light scattering and photoluminescence enhancement from plasmonic Vogel's golden spirals. *Laser Photon. Rev.* **11**, 1600235 (2017).
32. Iyer, P. P., Butakov, N. A. & Schuller, J. A. Reconfigurable semiconductor phased-array metasurfaces. *ACS Photon.* **2**, 1077–1084 (2015).
33. Das, T., Iyer, P. P., DeCrescent, R. A. & Schuller, J. A. Beam engineering for selective and enhanced coupling to multipolar resonances. *Phys. Rev. B* **92**, 241110 (2015).
34. Yu, N. et al. Light propagation with phase discontinuities: generalized laws of reflection and refraction. *Science* **334**, 333–337 (2011).
35. Taminiau, T. H., Karaveli, S., van Hulst, N. F. & Zia, R. Quantifying the magnetic nature of light emission. *Nat. Commun.* **3**, 979 (2012).
36. Schuller, J. A. et al. Orientation of luminescent excitons in layered nanomaterials. *Nat. Nanotechnol.* **8**, 271–276 (2013).
37. Kurvits, J. A., Jiang, M. & Zia, R. Comparative analysis of imaging configurations and objectives for Fourier microscopy. *J. Opt. Soc. Am. A* **32**, 2082–2092 (2015).
38. McGroddy, K. et al. Directional emission control and increased light extraction in GaN photonic crystal light emitting diodes. *Appl. Phys. Lett.* **93**, 103502 (2008).
39. Sell, D., Yang, J., Doshay, S., Yang, R. & Fan, J. A. Large-angle, multifunctional metagratings based on freeform multimode geometries. *Nano Lett.* **17**, 3752–3757 (2017).
40. Sandfuchs, O., Brunner, R., Pätz, D., Sinzinger, S. & Ruoff, J. Rigorous analysis of shadowing effects in blazed transmission gratings. *Opt. Lett.* **31**, 3638–3640 (2006).
41. Matioli, E. et al. High-brightness polarized light-emitting diodes. *Light Sci. Appl.* **1**, e22 (2012).
42. Faklis, D. & Morris, G. M. Diffractive optics technology for display applications. In *Proc. SPIE 2407, Projection Displays* (ed. Wu, M. H.) 57–61 (International Society for Optics and Photonics, 1995).
43. Piao, M.-L. & Kim, N. Achieving high levels of color uniformity and optical efficiency for a wedge-shaped waveguide head-mounted display using a photopolymer. *Appl. Opt.* **53**, 2180–2186 (2014).
44. Zhou, Q., Xu, M. & Wang, H. Internal quantum efficiency improvement of InGaN/GaN multiple quantum well green light-emitting diodes. *Opto-Electron. Rev.* **24**, 1–9 (2016).
45. Zhuang, Z. et al. Great enhancement in the excitonic recombination and light extraction of highly ordered InGaN/GaN elliptic nanorod arrays on a wafer scale. *Nanotechnology* **27**, 015301 (2016).
46. Wang, G. T., Li, Q., Wierer, J. J., Koleske, D. D. & Figiel, J. J. Top-down fabrication and characterization of axial and radial III-nitride nanowire LEDs. *Phys. Status Solidi* **211**, 748–751 (2014).
47. Xing, K., Gong, Y., Bai, J. & Wang, T. InGaN/GaN quantum well structures with greatly enhanced performance on a-plane GaN grown using self-organized nano-masks. *Appl. Phys. Lett.* **99**, 181907 (2011).

Methods

Growth and fabrication. The sample was grown heteroepitaxially on a (0001) *c*-plane double-side polished sapphire substrate by atmospheric pressure metal-organic chemical vapour deposition. The sample structure consisted of an AlGaN nucleation layer grown at 570 °C. A 1-μm unintentionally doped (UID) GaN template layer was grown at 1,200 °C. The active region consisted of three periods of multiple QWs with a 3-nm InGaN QW, a 2-nm $Al_{0.3}Ga_{0.7}N$ cap and a 10-nm GaN barrier. Finally, a 100-nm UID GaN protective buffer was grown on top that not only protects the emitting QW from fabrication damage but also provides the necessary boundary conditions for the emitted light to be channelled through the etched nanopillar into the substrate. Electron-beam lithography was done to generate the required metasurface patterns using hydrogen silsesquioxane (60-nm thick) as the resist on double hard-mask layers of ruthenium (30 nm) and SiO_2 (400 nm) on the GaN thin film. The hard masks were dry etched using an inductively coupled plasma etch using Cl_2/O_2 (at 100 W power) gas mixture for ruthenium and CHF_3/CF_4 gas mixture (at 50 W power) for SiO_2. Following the oxide etch, the ruthenium metal was dry etched away before the GaN etch in a reactive ion chamber. An initial BCl_3 etch at 100 W for 2 min was performed on the sample to remove the native oxide on the GaN (to prevent micro-masking) followed by a pure Cl_2 etch at 100 W power. This etch was developed to achieve extremely high-aspect-ratio GaN nanopillars (>40:1) with a vertical side-wall to etch through the 1.25-μm layer and stop on the sapphire substrate. The residual oxide hard mask was removed using a buffered HF dip for 60 s.

Transmission, PL and momentum-resolved PL. All transmission and PL spectra were measured using the home-built system illustrated in Supplementary Fig. 2. This system and measurement procedures are described in ref. [36]. Samples were optically pumped with uniform illumination through the objective using a 405-nm LED (ThorLabs M405L3). PL was collected through a 405-nm filter cube set (Semrock). Here, we define the sample coordinate system such that the entrance slit is parallel to the k_x axis ($k_y = 0$). An analysing polarizer was applied such that light along the k_x axis was either p- (x) or s- (y) polarized. To acquire conventional PL spectra (for example, Fig. 4c), we integrated energy-momentum spectra over all momenta within the numerical aperture (NA). Far-field patterns in Fig. 3 were produced using a band-pass filter that transmits between 525–535 nm.

Beam efficiencies. Experimentally measured metasurface transmission lobes exhibit clear minima flanking the main peak, making it easy to define the main lobe. The transmission efficiency is defined as the fraction of total power contained within the main lobe. In PL, no equivalent minima exist and we instead use the FWHM to define the main lobe. Note that the maximum possible PL beam efficiency defined in this manner is always less than 1. For instance, were all PL perfectly defined by a single Gaussian function with no side lobes, the beam efficiency would be 0.76.

PL quantum efficiencies. The EQE_{tot} of as-grown thin films and metasurfaces were measured in an integrating sphere by optically pumping samples with a 440-nm laser diode focused to the sample. The diode was driven with constant current above the lasing threshold and was varied between measurements such that the total optical output varied between ~200–350 mW (driving currents between ~400–700 mA). Total optical input was determined from measurements of the pump line with an empty integrating sphere. The focused spot has a FWHM of approximately 300 μm in the *y* dimension and a width of approximately 1 mm in the *x* dimension. For each data point, four such measurements were performed: (1) the pump line without an absorbing sample in place; (2) the pump line with absorbing sample in place; (3) the PL band with absorbing/emitting sample in place; (4) the PL band without absorbing/emitting sample in place. Measurement (4) was performed to quantify PL background levels. Total absorption was determined by subtracting (2) from (1). Similarly, total PL was determined by subtracting (4) from (3). The diode was driven at ~700 mA for approximately 10 min before all measurements to ensure stability of the optical output by minimizing thermal drift over the course of the measurements. The results reported in Fig. 4d were reproducible, albeit with small variations in the absolute numbers; in all trials, the metasurface shows higher EQE_{tot} than the as-grown thin films. EQE_{air} enhancements (Supplementary Section 1) were determined by integrating the collected PL (over all wavelengths and over all momenta within

NA = 1.0) for all samples using identical pump and collection conditions. No polarizer or spectral filters were used. The reported quantities fully account for variations in total absorption among samples. Absorption, *A*, was determined from transmission, *T*, and reflection, *R*, using the expression $A = 1 - T - R$; see Supplementary Section 1 for a further detailed description of absorption and PL enhancement measurements and calculations.

FDTD simulations. Numerical calculations were performed in Lumerical FDTD. For absorption enhancement calculations, a uniform pillar array with a 250-nm periodicity was simulated using periodic boundary conditions. Pillars (refractive index $2.4 + i0.001$, total height 1,450 nm) contained three absorbing layers (3-nm thick; refractive index $2.2 + i0.1$ in-plane, $2.2 + i0.001$ out-of-plane) representing the QWs at heights of 1,300 nm, 1,315 nm and 1,330 nm. Mesh sizes were kept at 4 nm × 4 nm × 6 nm in the bulk of the pillar and reduced to 4 nm × 4 nm × 0.5 nm in the absorbing layers. We assumed plane-wave illumination at normal incidence from the substrate and calculated total absorbed power in the QW layers by integrating the 'P_{abs}' (power absorbed) monitor spanning all QWs at 405 nm. Because absolute values depend on the assumed value of the imaginary part of the QW refractive index, we normalized all values by those for the thin film, thereby casting all reported values in terms of 'enhancements'. To estimate Purcell enhancements, we simulated large regions (12 μm × 12 μm in lateral extent, 2.07 μm height) of phased metasurface gratings with in-plane oriented electric dipole sources. Individual simulations were performed with the single-dipole source in each unique nanopillar within the macro-periodic supercell. Purcell factors were taken directly from dipole source results.

Data availability

The data that support the plots within this paper and other findings of this study are available from the corresponding author upon reasonable request.

Code availability

The code that supports the plots within this paper and other findings of this study is available from the corresponding author upon reasonable request.

Author contributions

P.P.I. and J.A.S. proposed, conceived and supervised the project. P.P.I., Y.M. and N.A.B. fabricated the devices. P.P.I. performed the numerical electromagnetics simulations and momentum-resolved luminescence measurements. R.A.D. performed momentum-resolved transmission and absorption measurements, and derived and coded the analytical LDOS model. R.A.D. and G.L. performed quantum efficiency measurements. G.L. performed the band structure calculation under the supervision of C.W. A.A. grew the quantum wells under the supervision of S.P.D. and S.N. P.P.I., R.A.D. and J.A.S. analysed the data. All authors contributed to the writing of the manuscript.

Competing interests

The authors declare no competing interests.

Additional information

Supplementary information is available for this paper at https://doi.org/10.1038/s41566-020-0641-x.

Correspondence and requests for materials should be addressed to J.A.S.

Reprints and permissions information is available at www.nature.com/reprints.